A Laboratory Perspective on the Gutenberg-Richter and Characteristic Earthquake Models

Evangelos Korkolis[1], André Niemeijer[2], Hanneke Paulssen[2], and Jeannot Trampert[3]

[1]University of Oslo
[2]Utrecht University
[3]Universiteit Utrecht

November 24, 2022

Abstract

Probabilistic seismic hazard analysis (PSHA) is the standard method used for designing earthquake-resistant infrastructure. In recent years, several unexpected and destructive earthquakes have sparked criticism of the PSHA methodology. The seismological part of the problem is the true frequency-magnitude distribution of regional seismicity. Two major models exist, the Gutenberg-Richter (G-R) and the Characteristic Earthquake (CE) model, but it is difficult to choose between them. That is because the instrumental, historical, and paleoseimological data available are limited in many regions of interest. Here we demonstrate how a friction experiment on aggregates of glass beads can produce both regular (CE equivalent) and irregular (G-R equivalent) stick-slip. Using a new rotary shear apparatus we produced and analysed large catalogs of acoustic emission (AE) events related to stick-slip. The distributions of AE sizes, interevent times and interevent distances were found to be sensitive to particle size and the applied normal stress, and, to a lesser degree, the stiffness of the loading apparatus. More importantly, the system spontaneously switched behavior for short periods of time. In the context of PSHA, if faults are able to switch behavior as our experimental system does, then justifying the choice of either the CE or the G-R model is impossible based on existing observations.

A Laboratory Perspective on the Gutenberg-Richter and Characteristic Earthquake Models

Evangelos Korkolis[1,2], André R. Niemeijer[1], Hanneke Paulssen[1], Jeannot Trampert[1]

[1]Department of Earth Sciences, Utrecht University, The Netherlands
[2]Now at: Njord Centre, University of Oslo, Norway

Key Points:

- A frictional interface can produce both characteristic and power-law distributed instabilities
- The system can alternate between the two regimes
- Choosing a fault-specific frequency-magnitude distribution may require longer seismicity catalogs than currently available

Corresponding author: André R. Niemeijer, `A.R.Niemeijer@uu.nl`

Abstract

Probabilistic seismic hazard analysis (PSHA) is the standard method used for designing earthquake-resistant infrastructure. In recent years, several unexpected and destructive earthquakes have sparked criticism of the PSHA methodology. The seismological part of the problem is the true frequency-magnitude distribution of regional seismicity. Two major models exist, the Gutenberg-Richter (G-R) and the Characteristic Earthquake (CE) model, but it is difficult to choose between them. That is because the instrumental, historical, and paleoseimological data available are limited in many regions of interest. Here we demonstrate how a friction experiment on aggregates of glass beads can produce both regular (CE equivalent) and irregular (G-R equivalent) stick-slip. Using a new rotary shear apparatus we produced and analysed large catalogs of acoustic emission (AE) events related to stick-slip. The distributions of AE sizes, interevent times and interevent distances were found to be sensitive to particle size and the applied normal stress, and, to a lesser degree, the stiffness of the loading apparatus. More importantly, the system spontaneously switched behavior for short periods of time. In the context of PSHA, if faults are able to switch behavior as our experimental system does, then justifying the choice of either the CE or the G-R model is impossible based on existing observations.

1 Introduction

Probabilistic seismic hazard analysis (PSHA) is currently the standard tool for designing earthquake-proof infrastructure (Stirling, 2014). Recently, the unexpected occurrence of destructive earthquakes such as the 2011 M_w 9.1 near Tohoku, Japan, has been interpreted by some authors as failure of the PSHA approach (Geller et al., 2015; Mulargia et al., 2017; Stein et al., 2011, 2012; Stein & Friedrich, 2014). The disparity between expectation and reality has been largely attributed to epistemic uncertainty regarding the physics of seismicity (Stein et al., 2012). A prime example is the uncertainty regarding the shape of the frequency-magnitude distribution (FMD); more specifically its right-hand side tail, that contains the largest and most devastating earthquakes.

Seismologists face the challenge of not knowing the true FMD of earthquake-prone areas. Instead, they rely on seismic records collected since the dawn of instrumental seismology, approximately 100 years ago, and supplemented by paleoseismological studies to produce empirical FMDs. Thus two main types of FMDs have been proposed: the Characteristic Earthquake (CE) model and the modified Gutenberg-Richter (G-R) model (Schwartz & Coppersmith, 1984; Kagan, 1994, 1996; Wesnousky, 1994). Use of the wrong FMD in seismic hazard analysis could lead to under- or over-estimation of the maximum expected magnitude and the rate of large earthquakes.

According to the modified G-R model, the logarithm of the cumulative number of earthquakes above a certain magnitude is a linear function of magnitude with a slope of approximately -1 (Kanamori & Brodsky, 2004). In practice the probability density of seismic moment is best described by a gamma distribution, i.e. a power law with an exponential right-hand side tail (Kagan, 1994; Main, 1996; Sornette & Sornette, 1999). The G-R model is well supported by data from global and regional seismicity, but its universality on regional scales is disputed by some authors, who posit that large earthquakes on individual faults and plate boundary segments occur quasi-periodically and typically with a small range of magnitudes (Schwartz & Coppersmith, 1984; Wesnousky, 1994). Such events are also known as “dragon-kings” (Sachs et al., 2012; Sornette & Ouillon, 2012). The concepts of characteristic earthquakes and seismic gaps are intimately linked. Seismic gaps are a corollary of plate tectonics and elastic rebound: if most of the slip along plate boundaries occurs seismically, then earthquakes are likely to occur in regions where there is slip deficit. Assuming constant plate motion, i.e. a constant loading rate on the “locked” boundaries, seismic slip should occur quasi-periodically and with “fixed” magnitude so as to cover the slip deficit in that particular “gap” or segment of the plate boundary, followed by a reloading period and another characteristic earthquake, giving rise to the so called “seismic cycles.”

The idea of characteristic earthquakes and seismic gaps has been applied to various hotspots of natural seismicity, both onshore and offshore. A classic onshore application has been the North Anatolian Fault in Turkey (Barka, 1996; Toksöz et al., 1979). Offshore, seismicity on Gofar, a mid-ocean ridge transform fault in the East Pacific Rise, has been interpreted as an example of seismic cycles. This motivated the timely deployment of ocean bottom seismometers to capture a 2008 Mw 6.0 earthquake along with its foreshocks and aftershocks (Boettcher & McGuire, 2009; McGuire, 2008; McGuire et al., 2012; Wolfson-Schwehr et al., 2014). A similar attempt in Parkfield, California, where earthquakes had been occurring every approximately 20 years since the mid 19th century, was unsuccessful (Bakun & Lindh, 1985; Kagan et al., 2012; Savage, 1993). Nevertheless, the characteristic earthquake model appears to be a key ingredient of modern rupture forecasts for California (Field et al., 2017; Parsons et al., 2018) and has been used to calculate earthquake probabilities in Japan (Parsons et al., 2012). The idea of quasi-periodic earthquakes of a characteristic magnitude has understandably gained traction with seismic hazard analysis because it places constraints on “where”, “when”, and “how big” for large earthquakes.

Despite its appeal and popularity, the CE model has been found to perform poorly in comparison with the G-R model and random chance, and forecasts based on it have been criticized for being largely untestable (Kagan, 1993; Kagan & Jackson, 1991, 1995, 1999; Parsons & Geist, 2009; Rong et al., 2003). More recently, earthquakes such as the 2011 M_w 9.1 near Tohoku, Japan and 2016 M_w 7.8 near Kaikoura, New Zealand challenge a basic assumption of seismic gaps and characteristic earthquakes, i.e. that only one fault or plate boundary segment can rupture in an earthquake (Furlong & Herman, 2017; Kagan & Jackson, 2013; Lamb et al., 2018; Shi et al., 2017). Considering the long recurrence time of large earthquakes, often in the hundreds of years, the length of the instrumental record of earthquakes (approximately 100 years) and the limitations of paleoseismological research (Weldon et al., 2004), it is not clear whether characteristic earthquakes and seismic gaps are real features or artifacts of small data sets. The problem is worse for intraplate regions, where the time between large earthquakes is longer than the average occurence rate at plate boundaries (Stein et al., 2012). Synthetic tests using randomly generated earthquakes along the eastern coast of Canada or the North Africa plate margin have shown that a limited window of observation (order of 10^3 years) can lead to the false impression of seismic gaps and characteristic earthquakes (Swafford & Stein, 2007).

The epistemic uncertainty regarding earthquake physics and the problem of data sparsity have motivated theoretical, numerical, and laboratory studies that aim to simulate the complexity of natural seismicity (Shcherbakov et al., 2015). The intermittent style of deformation that such artificial systems exhibit has striking similarities with natural seismicity, such as power-law scaling of event sizes and Omori-type correlations in the time domain. Characteristic events or G-R type behavior can be reproduced by Burridge-Knopoff type spring-block models (Brown et al., 1991; Carlson & Langer, 1989), Lattice-Boltzmann models (Benzi et al., 2016), cellular automata and rupture mechanics models (e.g., Ben-Zion & Rice, 1993, 1995; Dahmen et al., 1998; Klein et al., 2017), discrete element method simulations (e.g., van den Ende et al., 2018; Ferdowsi et al., 2013), and laboratory experiments (e.g., Anthony & Marone, 2005; Baró et al., 2013; Dalton & Corcoran, 2001, 2002; Hamilton & McCloskey, 1997; Hayman et al., 2011; Johnson et al., 2013; Mair et al., 2002; Jiang et al., 2017).

Here we present the statistics of acoustic emission (AE) events from large displacement rotary shear experiments on thin layers of glass beads. AEs are a byproduct of the intermittent deformation of the granular samples. By imposing large total displacement, our system generated large numbers ($\sim 10^4$) of AE events. Unlike catalogs of natural seismicity, that contain unique sequences and are usually short compared to the inferred recurrence intervals of large events, catalogs generated via our laboratory experiments are both reproducible and can be arbitrarily long. We show that by tuning certain parameters of the experiment, namely the particle size distribution and the normal stress, we were able to produce both CE and G-R type distributions. The role of system stiffness has a less clear effect. We also show that the system is able to temporarily switch behavior between the two types, likely due to the evolution of sample-related properties. These findings imply that justifying the choice of a FMD for individual faults is impossible with the amount of seismological data available at the moment. Lastly, this contribution fills a literature gap that exists between studies presenting experiments with large total displacement under very low normal stress (<< 1 MPa) (e.g., Dalton & Corcoran, 2001, 2002; Jiang et al., 2017; Cui et al., 2017), and studies reporting on experiments with short total displacement (< 50 mm) under normal stresses of a few MPa. (e.g., Mair et al., 2002; Anthony & Marone, 2005; Scuderi et al., 2015).

2 Methods

We generated laboratory quake catalogs by shearing thin layers of soda-lime glass beads in a rotary shear apparatus. We applied a constant rate of rotation ($0.02^o/s$) and constant normal stress, at room temperature and relative humidity (see Table 1). The starting layer thickness was approximately 4.5 mm. The sample material consisted of two batches of soda-lime glass beads with size ranges of 150 to 212 μm and 400 to 500 μm respectively. We chose glass beads as the sample material because their aggregates exhibit stick-slip behavior and produce AE when sheared at room temperature conditions and at load point velocities relevant for seismic nucleation (<100 μm/s). Furthermore, it is a well-studied material that has been used in numerous laboratory studies before (e.g., Anthony & Marone, 2005; Mair et al., 2002; Scuderi et al., 2014, 2015; Nasuno et al., 1997; Jiang et al., 2017). In addition, the spherical shape of the beads is a close physical analog to the disk-shaped and spherical particles commonly used in discrete element method studies of sheared granular aggregates (e.g., Mair & Hazzard, 2007; Morgan & Boettcher, 1999; Morgan, 1999, 2004; Guo & Morgan, 2007). This allows comparisons between experiments and discrete element method simulations to be made.

2.1 Rotary Apparatus (RAP)

For this study, we used a newly developed rotary shear apparatus (Figure 1). The main advantage of the rotary shear configuration is that it can impose arbitrarily large shear displacements, unlike the other common experimental configurations, namely the (double) direct-shear and triaxial compression. The apparatus is housed inside an Instron 8862 testing machine equipped with a servo-controlled electromechanical actuator that may be operated either in position control (±50 mm range, 5 μm resolution) or in load control mode (±100 kN range, 0.008 kN resolution). An additional torque reaction frame resists the moment that is developed during operation. A Parker MH205 motor provides rotary motion to the driving plate via a 1:160 harmonic drive gearbox. Using the motor's onboard servo-controller, it is possible to control either the rotation rate (and thus shear displacement) or the torque (and thus the shear stress) imposed by the driving platter. In this study, we applied a constant rate of rotation. The driving platter is equipped with two potentiometers (0.001 degrees, or about 0.74 μm resolution) that measure its rotation. A pair of load cells (20 kN range, 0.008 kN resolution), mounted on opposite sides of a horizontal steel block ("crosshead"), measure the reaction force of the frame due to the rotation imposed by the motor. The reaction force is used to calculate the shear stress, τ, on the sample, as will be described later in this section. Axial displacement (i.e. dilation or compaction of the sample) is measured in two ways. First, by an external linear variable differential transducer (LVDT; ±0.5 mm range, 0.1 μm resolution), installed at the side of the frame, at the height of the sample chamber. Second,

Table 1. Table of experiments. The numbers of AE events exclude the run-in period of 1000 s (20^o). RH: relative humidity. h_0 & h_f: starting & final thickness of the sample. ρ_0 & ρ_f : initial & final bulk density.

Experiment ID	Particle Size Range	σ_n (MPa)	Torsional Stiffness	T (^oC)	RH (%)	Sample Mass (g)	h_0 (mm)	h_f (mm)	ρ_0 (g/cm^3)	ρ_f (g/cm^3)	Max. Displacement (^{o}; mm)	Number of AE Events
r054	150-212	8	High	24	61	30.00	4.35	3.89	1.7	1.9	193.0; 143.2	10316
r080	150-212	8	High	23	69	30.11	4.41	3.78	1.7	2.0	193.2; 143.3	19048
r082	150-212	8	High	23	69	30.15	4.28	3.88	1.8	1.9	195.4; 144.9	12207
r055	150-212	8	Low	25	69	30.00	4.30	4.16	1.7	1.8	195.2; 144.8	13392
r066	150-212	4	Low	23	72	30.00	4.46	4.21	1.7	1.8	200.3; 148.6	9452
r068	150-212	4	High	24	72	30.00	4.41	3.98	1.7	1.9	202.4; 150.1	9201
r086	400-500	8	High	23	62	30.20	4.40	3.60	1.7	2.1	195.0; 144.6	38699
r097	400-500	8	High	23	50	30.20	4.75	3.61	1.6	2.1	222.2; 164.8	48699
r101	400-500	8	High	20	51	30.20	4.40	3.79	1.7	2.0	234.4; 173.8	49045
r103	400-500	8	High	20	50	30.20	4.35	3.80	1.7	2.0	222.6; 165.1	33567
r114	400-500	8	Low	21	46	30.20	4.41	3.64	1.7	2.1	225.9; 167.6	34040
r107	400-500	4	High	20	26	30.20	4.41	4.36	1.7	1.7	229.4; 170.2	8246

using the built-in position sensor of the Instron, with a resolution that is comparable to that of the external LVDT. All of the resolution values reported here have been calculated with the respective transducer(s) at constant load or constant position, at steady state conditions, as six standard deviations. A PT100 thermocouple was used to monitor the ambient temperature. A wall-mounted Fischer thermometer-hygrometer was used to measure the ambient relative humidity. Mechanical data were logged at 10 kHz in streaming mode, whereas AE events were logged at 5 MHz, in block mode. Both types of data were acquired by an ELSYS TraNET EPC, thereby ensuring a common time base.

The operation of the apparatus can be captured conceptually by a simplified direct-shear system, such as the one shown in Figure 2. Loading a sample until failure produces shortening of the upper section of the plot (gearbox, pistons, sample, crosshead) and stretching of the lower section (frame). At failure, the system unwinds as the elastic energy stored in its various components is released. We can increase the amount of elastic energy that the system can store by lowering the effective spring constant of the crosshead. In the real machine, this is done by replacing the stiff mounting points of the load cells onto the crosshead by sets of Belleville washers. In this study, the stiff mounting points have an effective spring constant of approximately 1800 kN/mm, whereas the compliant ones have an effective spring constant of about 0.82 kN/mm; a ratio of 2195:1 between the two configurations.

2.2 Experimental Procedure

Prior to each experiment, a known mass of the sample material, was funneled into the annular cavity formed by the bottom piston ring (outer diameter: 100 mm; inner diameter: 70 mm) together with the inner and outer confining rings. The amount of sample used was chosen such that the initial thickness of the resulting layer would be about 4.5 mm, at around 40% initial porosity. The layer was flattened using a ring-shaped aluminum block and a bull's eye level was used to verify the result. The top piston ring was then installed, closing the annular cavity. The two piston rings have serrated surfaces (teeth height 200 μm; average spacing about 0.5 mm) to improve the grip onto the sample. The height of the sample assembly was measured ($\pm$0.05 mm) in four locations at 90-degree intervals and the relative offset of two reference points, one on the top piston and one on the bottom piston, was calculated by measuring their respective azimuths using a repurposed microscope stage ($\pm 0.5^0$ resolution). Subsequently, all 16 AE transducers were installed, and the sample assembly was placed into the apparatus, with the bottom piston interlocking with the driving platter. The actuator was then moved upwards, lifting the driving platter and the sample assembly up and interlocking the top piston with the crosshead. After establishing contact axially, the actuator was switched to load control mode and the target total normal load was applied gradually over a period of 60 s. The normal stress values used (4 and 8 MPa) are below the threshold (25 MPa) of pervasive fracturing regime for soda-lime glass beads (Mair et al., 2002). To shear the sample at a constant rate, clockwise rotation was applied via the MH205 motor for about 3 hours. By the end of shearing, the accumulated displacement (in excess of 190 degrees or 140 mm) was much larger than the initial thickness of the sample (4.5 mm). At that point, a brief counter-clockwise rotation (2^0-3^0) was performed to remove the remaining shear stress. Subsequently, normal stress was reduced gradually, over a period of 60 s. After the experiment, the height of the sample assembly and the relative angular offset between the two pistons were measured again. Finally, the sample was retrieved and in certain cases prepared for particle size analysis and observation with a table-top scanning electron microscope (SEM).

2.3 Data Processing

In this study we make use of the following quantities: the apparent coefficient of friction, or simply "friction" of the samples, the size and 1D source location (azimuth)

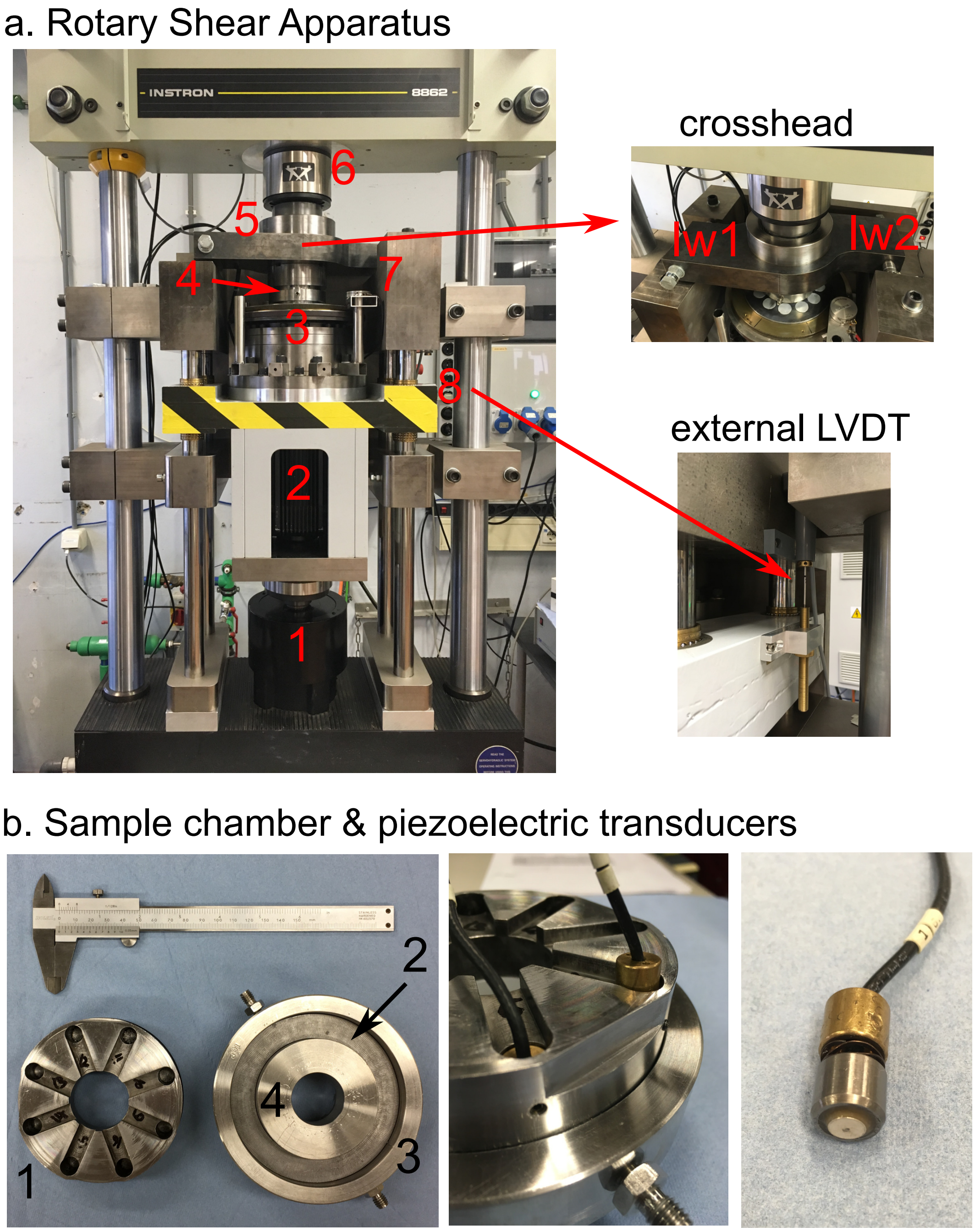

Figure 1. (a) View of the Rotary shear Apparatus (RAP). 1: Instron actuator. 2: MH205 motor. 3: Harmonic drive and rotating platter. 4: Sample chamber. 5: Crosshead, equipped with two load cells (lw1, lw2) for measuring traction. 6: Instron load cell. 7: Angular potentiometer (1 of 2). 8: external LVDT. (b) Sample chamber and piezoelectric transducers. (b, left) 1: Top piston. 2: Bottom piston. 3: Outer ring with two fluid ports. 4: Inner ring. The outer diameter of the sample cavity is 10 cm and the inner diameter 7 cm. 150 mm caliper for scale. (b, middle) close-up view of the assembled sample chamber. One piezoelectric transducer has been properly installed (left), whereas a second one has been partially inserted into its slot. A small screw is used to fix the brass cap against the steel piston. (b, right) A piezoelectric transducer. The piezoelectric element (white disk) is 5 mm in diameter. The casing has an outer diameter of 10 mm. When installed, the piezoelectric elements lie approximately 5 mm away from the sample. Figure from Korkolis (2019).

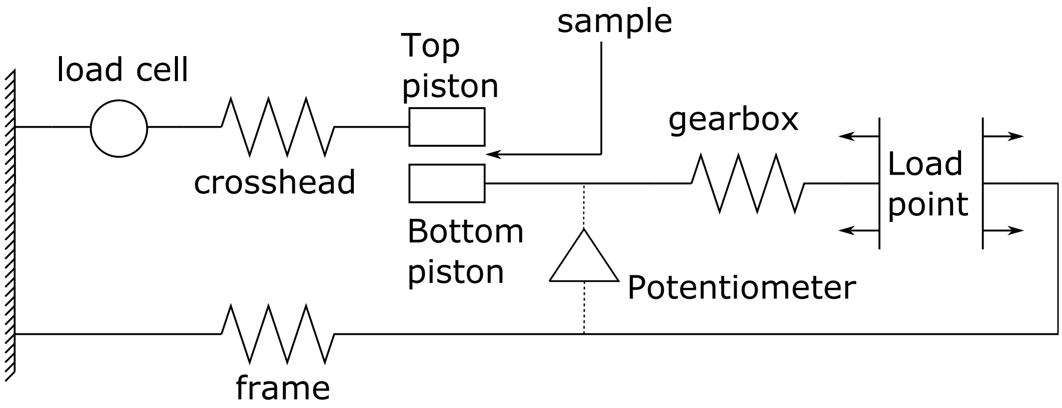

Figure 2. Simplified mechanical model of the apparatus. Aside from the sample, mechanical elements that contribute the most to the stiffness of the system are shown as springs. The circle represents the pair of load cells mounted inside the crosshead. The triangle represents the two potentiometers that measure the rotation of the bottom piston relative to the frame. To lower the shear (torsional) stiffness of the system, we added sets of Belleville washers inside the crosshead where the load cells are mounted. Modified after Korkolis (2019).

of the AE events, as well as the interevent time and angular distance. We calculated the apparent coefficient of friction as the ratio of shear stress to normal stress. Shear stress was calculated by converting the time series of the force F_r recorded by the two load cells installed in the crosshead, to shear force on the sample and dividing by the surface area of the piston ring, via:

$$\tau_r = \frac{F_r * r_{ch}}{r_{mean} * A} \tag{1}$$

where A, r_{mean} are the surface area and mean radius of the sample, and r_{ch} the radius of the crosshead. As the normal stress was servo-controlled, variations in friction largely reflect variations in shear stress. We define the size S of an AE event as shown in the following formula:

$$S = \sum_{i=1}^{16} E_i \tag{2}$$

where E_i is proportional to the energy contained in the signal recorded by the i^{th} transducer, and can be calculated using the following formula, after Baró et al. (2013):

$$E_i = \int_0^T |x(t)|^2 dt \tag{3}$$

where $x(t)$ is the time series of voltage, with duration T. Note that E_i is measured in V^2s, rather than J.

We estimated 1D source locations of acoustic emission events by automatically picking first arrival times of the fast, longitudinal waves and inverting them for minimum time-of-flight (t), source location azimuth (θ), and apparent wave propagation velocity (v). A single velocity model was assumed, based on the fact that the dominant wavelength of the AE waveforms is larger or at least comparable to the distance between the sample and the nearest AE transducers. We define the minimum time-of-flight t as the time-of-flight from the source to the receiver that records the earliest arrival. The source location (θ) is expressed as the azimuth along the circumference of the sample, referenced to the top, stationary piston. We chose to solve for one spatial dimension instead of three (r, θ, z) because the estimated errors in the radial and vertical dimensions (r and z respectively) are comparable to the sample size in those dimensions (radial size of the sample: 15 mm; sample height: between 5 mm and 2 mm, depending on the initial height and the amount of compaction during the experiment). Therefore, we fixed $r = 42.5$ mm and $z = 0$ mm, with zero height representing the middle of the sample. Tests using calcite powder, a material that exhibits stable sliding and does not produce AE under the same experimental conditions, revealed that the apparatus does not produce detectable signals. Thus, all of the AE events recorded during the experiments discussed here must have originated from within the aggregates. Details of the procedure for picking first arrivals and inverting for the source location are given in Appendix A.

The complete recovery of samples r086, r097, r101, and r103 allowed post-mortem analyses to be performed on them. Particle size analysis was performed using a Mastersizer S device. We present the results as percent volume of each fraction versus the logarithm of particle size in micrometers. Scanning electron photomicrographs of particles from r086 were obtained using a JEOL JCM-6000 tabletop SEM.

3 Results

All of the samples exhibited stick-slip behavior and net compaction (Table 1). We did not observe systematic net weakening or strengthening trends in our experiments. The top panels in Figure 3 show representative examples from two experiments at 8 MPa normal stress, r054 (small particles) and r086 (big particles). Regular stick-slip was the dominant behavior in r054. In r086 we observed mainly irregular stick-slip. Both experiments show transitions between regular and irregular stick-slip. Here, we use the term regular stick-slip to describe CE-type quasi-periodic instabilities that typically have the same magnitude. With the term irregular stick-slip we refer to data that contain G-R-type aperiodic instabilities that have a wide range of magnitudes. We did not observe any complete stress drops.

The bottom panels of Figure 3 show the source locations of the corresponding AE activity. AE sources were spread all along the ring-shaped samples. Isolating the parts of the shear stress time series that correspond to the durations of the AE events, we found that some portion of AEs are associated with measurable changes in shear stress; mainly stress drops. For the rest of the AE events there are no significant fluctuations in the shear stress data.

More details of individual slip events can be seen in some representative data from r103, shown in Figure 4. The three largest stress drops are associated with changes in sample height, fast slip, and large AE events. For smaller stress drops the association with volumetric changes and slip is less clear. For some AE events there are no detectable changes in the mechanical data.

One way to quantify and illustrate the two types of stick-slip (regular versus irregular) is by plotting the empirical probability densities of AE sizes and interevent times. Figure 5 shows the probability density distributions of AE sizes, $f(S)$. The data are grouped by experimental conditions, namely normal stress (σ_n), particle size range (150-212 μm or 400-500 μm), and torsional stiffness. One common feature of all distributions is the linear part between 2×10^{-5} V^{2}s and 10^{-3} V^{2}s. This limited (almost 2 decades) linear part in the log-log plot represents a power law and has been observed in similar experiments under lower normal stresses (e.g., Dalton & Corcoran, 2001; Uhl et al., 2015; Lherminier et al., 2019; Geller et al., 2015). The shape of the distributions for smaller sizes suggests the influence of finite detection limits, with an apparent size of completeness $S_c = 2{\times}10^{-5}$ V^{2}s. More interestingly, the scaling of large events (S > 10^{-3} V^{2}s)

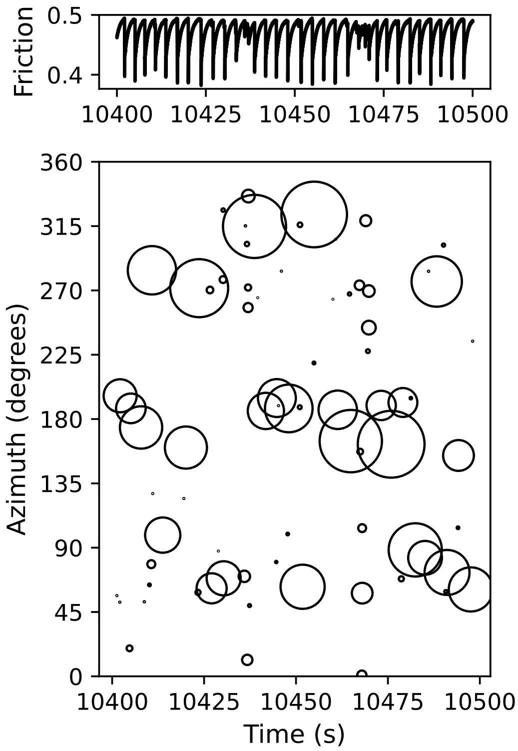

Figure 3. Friction data (shear/normal stress) and AE source locations from two experiments performed under the same conditions but using different particle size ranges. On the left: r054 (150-212 μm). On the right: r086 (400-500 μm). In the bottom panels, the diameter of the circles scales with the size of the AE event.

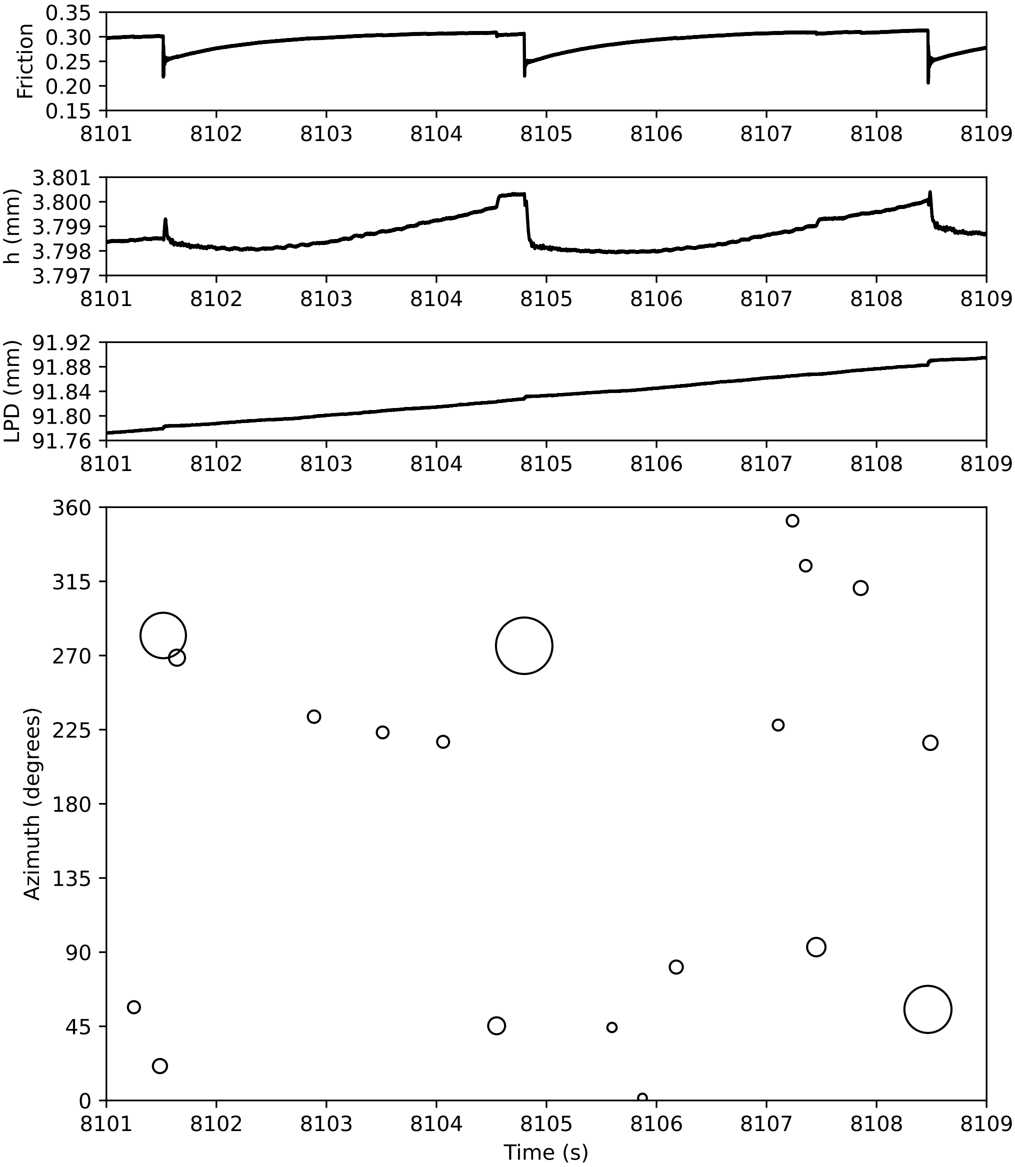

Figure 4. Data from experiment r103 ($\sigma_n = 8$ MPa, large particles). From top to bottom: friction, sample height, load point displacement and azimuth of AE events versus time. Figure from Korkolis (2019).

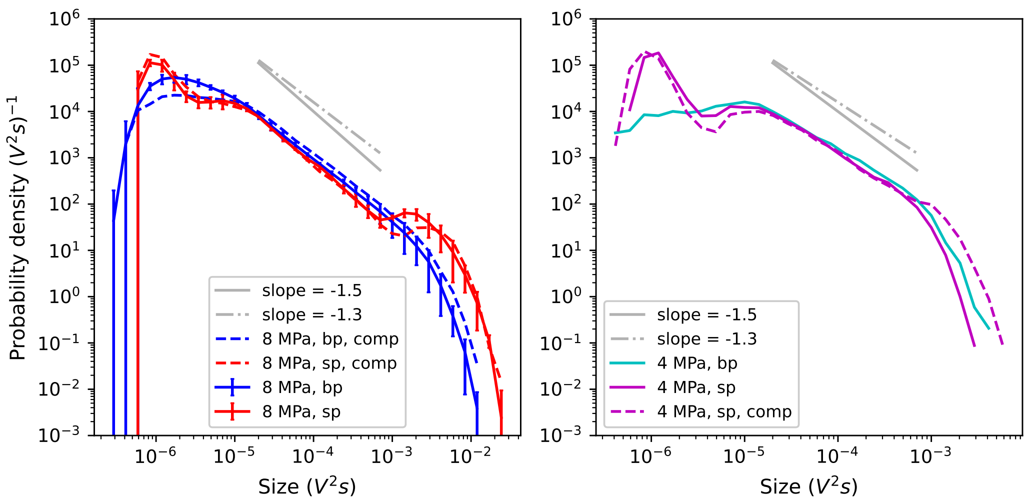

Figure 5. Probability density distributions of AE sizes. "bp": big particles; "sp": small particles; "comp": compliant configuration. The average probability density curves and two standard deviations (vertical bars) are shown for the replicated experiments using the stiff configuration, 8 MPa normal stress, small particles (r054, r080, r082) and big particles (r086, r097, r101, r103). On the left plot, notice the relative abundance of large events for the red curves as opposed to the blue ones. Intermediate size events for all experiments scale linearly for approximately two decades.

also deviates from the power law seen in the intermediate size range. For the majority of the experiments we see an exponential drop in the right-hand side tail of the distributions. For experiments on small particles under $\sigma_n = 8$ MPa, however, we found a relative abundance of large events (Figure 5, left panel). The effect of torsional stiffness is not clear. Our data from experiments at $\sigma_n = 4$ MPa indicate that reducing the torsional stiffness results in a small increase in the number (and size; see the right panel in Figure 5) of large events. Finally, increasing the normal stress allowed the system to produce larger AE events.

Regular and irregular stick-slip are also reflected in the normalized interevent time distributions, ($f(R\Delta t)$), shown in Figure 6. Here, R is the mean rate of recurrence, computed as the number of AE events above a certain threshold, divided by the duration of the experiment. We set the threshold value equal to S_c. The distributions for stiff and compliant configurations collapse and none of them appears to be exponential. For large particles under high normal stress, the density curves clearly follow a generalized gamma distribution (linear scaling at the shorter times with an exponential right-hand side tail), which implies non-trivial space-time correlations in the system (Kumar et al., 2020). Data from small particles show steeper scaling of short $R\Delta t$ than those from large particles, regardless of normal stress. The curves for the experiments on small particles at $\sigma_n = 8$ MPa have a clear peak near $R\Delta t = 2.5$. A smaller peak can be seen for $\sigma_n = 4$ MPa.

To determine whether there is clustering of AE source locations, we computed the distance $\Delta\theta = (\theta_{i+1} - \theta_i)$, in degrees (^{o}), between the source locations θ_i and θ_{i+1} of consecutive AE events i and i+1. The probability densities, calculated using a bin size of 10^o (as opposed to the mean uncertainty of source locations, $\pm 3.5^o$) are shown in Figure 7. As was the case with the distributions of event sizes and interevent times, the effects of normal stress and particle size range are more obvious than the effect of lower-

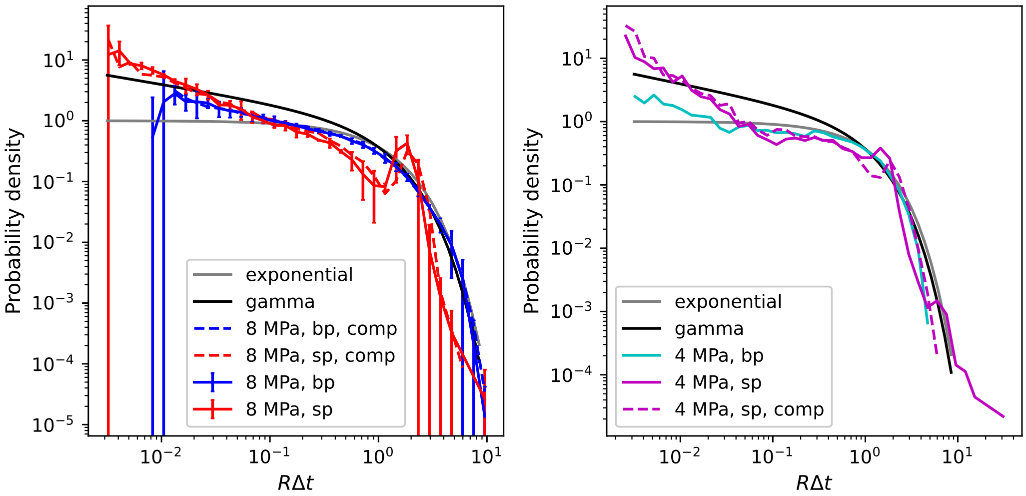

Figure 6. Probability density distributions of recurrence times Δt. The naming and coloring scheme follow the convention of Figure 5. The vertical bars on the left panel indicate ± 2 standard deviations from the mean, for replicated experiments. None of the distributions appears to be exponential and the red ones on the left plot have a peak at approximately 2.5 s.

ing the torsional stiffness. The curves corresponding to experiments on small particles show greater clustering at smaller interevent distances, compared to their large particle counterparts.

The samples remained completely confined during the experiments and no extrusion was observed. Post-experiment visual examination of the samples showed evidence of particle size reduction in the form of very fine powder. The concentration of powdered material was consistently higher along the boundary between the sample and the rotating piston, forming a cohesive layer. While most particles retained their original size, experiments at 8 MPa normal stress generated a larger amount of fine particles than those at 4 MPa. Particle size analysis on selected portions of the fully salvaged samples from r086, r097, r101, and r103 showed that a significant amount of the fines has a particle size of about 75 μm (Figure 8, top left). SEM photomicrographs of glass beads from r086 (Figure 8; panels a, b, and c) show that particles were damaged to varying degrees. The majority of the inspected particles showed evidence of surface wear only. Very few particles had been fragmented.

4 Discussion

The choice between the characteristic earthquake and the Gutenberg-Richter models is critical to the effectiveness of probabilistic seismic hazard analysis maps: it reveals the expectation of the map makers about the rate at which large earthquakes occur in the region of interest. If the characteristic earthquake model is the true one, but the G-R model is chosen instead, PSHA will underestimate the rate of large earthquakes, perhaps resulting in a costly recovery should a disaster occur. If, however, seismicity follows the G-R law, but the characteristic earthquake model is chosen instead, PSHA will overestimate the rate of large earthquakes, which may result in unnecessary expenses for disaster prevention. The complex nature of natural seismicity, combined with the limited instrumental record, and the limitations of paleoseismology, make it difficult to decide which model is the correct one.

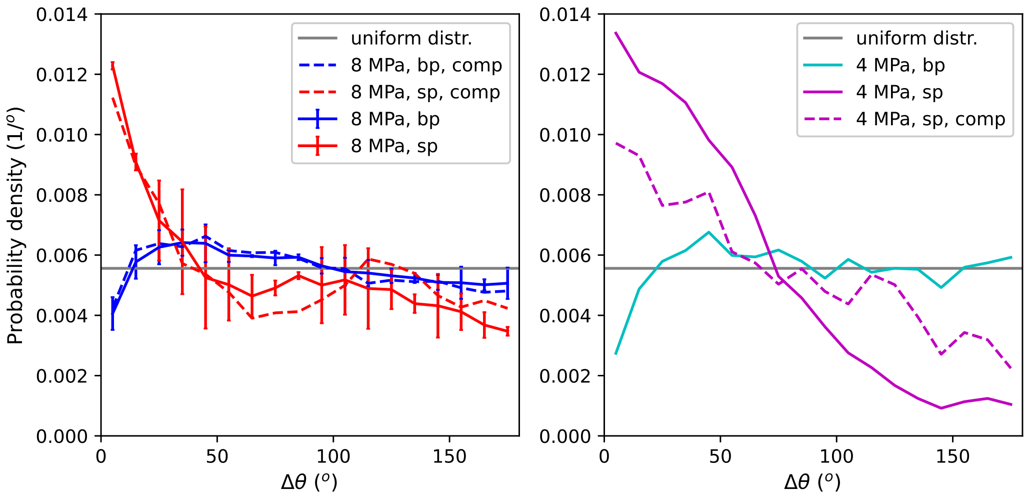

Figure 7. Probability density distributions of $\Delta\theta$. Bin size is 10^o. The horizontal gray line shows the probability density of the uniform distribution. The naming and coloring scheme follow the convention of Figure 5. The vertical bars on the left panel indicate ± 2 standard deviations from the mean, for replicated experiments. The distributions representing small particles deviate from uniformity more so than the distributions representing big particles.

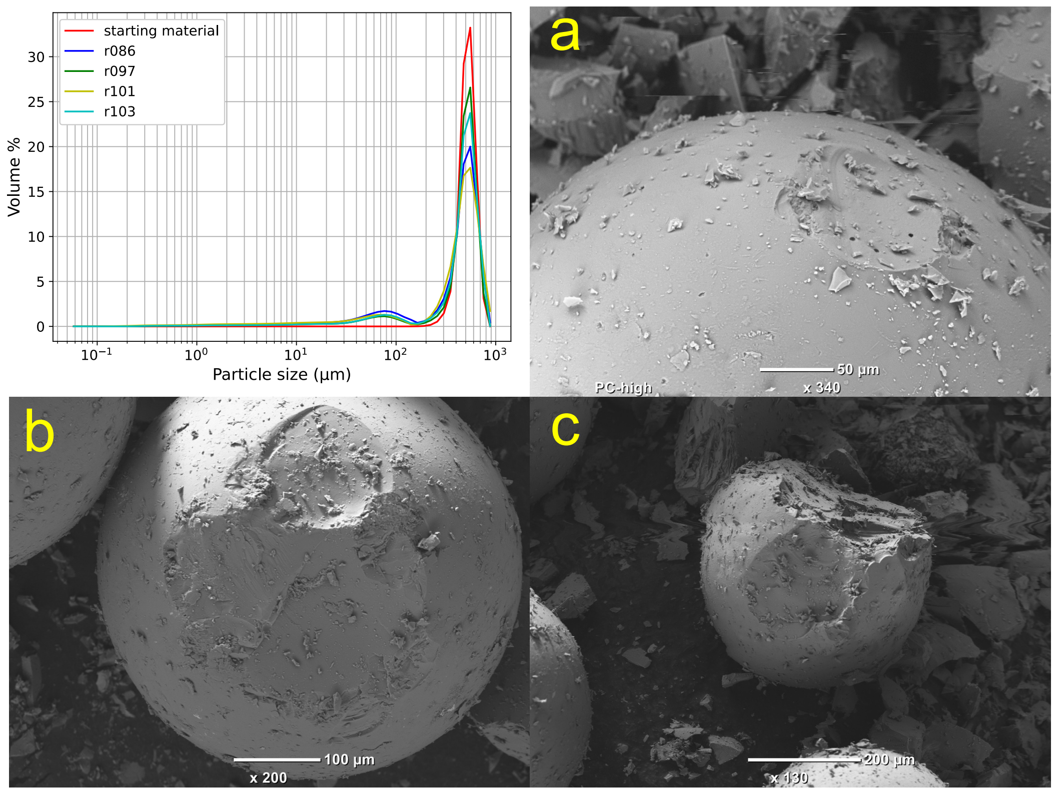

Figure 8. (top left) Particle size analysis of the starting material (red) and of the salvaged samples (colored). Note the appearance of particles smaller than 150 μm in the salvaged samples. These particle sizes were not present in the starting material. (a, b, c) Post-experiment SEM micrographs of damaged glass beads from sample r086. The flakes covering the beads are a by-product of frictional wear. Modified after Korkolis (2019).

4.1 System Physics

We have presented a mechanical system that produces a variety of complex mechanical behaviors and acoustic signatures when loaded at a “slow”, constant rate. The data presented here show that by using small or big particles for the thin granular layer that forms the frictional interface, and applying an elevated normal stress value, we can obtain either characteristic event or truncated power law distributions of avalanche sizes, as quantified by analyzing their acoustic signature. Both types of samples occasionally transition to brief periods of atypical deformation (e.g. samples consisting of large particles, that typically exhibit irregular stick-slip behavior, occasionally experience brief periods of regular stick-slip). Lowering the torsional stiffness of the apparatus produced subtler effects.

The synchronous occurrence of stress drops and AE events suggests that AEs were generated at the nucleation sites of slip instabilities, when sudden displacements, translations, or limited fracturing of particles resulted in the generation of elastic waves. Using mechanical and AE data sampled at 1 MHz, Jiang et al. (2017) found that in their ring shear experiments on glass beads, the origin time of AE events preceeded the onset of stress drops by several milliseconds. We assume that the particles involved in the nucleation of instabilities were members of force chains, i.e. the load-bearing structures in stressed granular media (e.g., Jaeger et al., 1996; Cates et al., 1998). According to the SEM microphotographs of particles from several of our experiments, as well as similar evidence from the findings of Scuderi et al. (2015); Jiang et al. (2017); Cui et al. (2017), the collapse of the force chains occurred mainly due to abrasive wear of load-bearing particles.

Are AEs generated by slip events that span the entire sample or only parts of it? For those AE events that are associated with a stress drop, the answer is clearly ”sample-wide” (Figure 4). For the rest, there is no definitive answer yet. Some may be associated with tiny stress drops that are below the detection threshold of the load cells. However, we cannot preclude that some AE events may not be associated with any stress drops and thus be local events. Further light might be shed on the question by lowering the detection threshold of shear stress (i.e. torque) drops and by studying the shape and frequency content of the AE waveforms to infer the source size. This is left as future work.

The linear portion seen in the AE size distributions (Figure 5) suggests that energy dissipation is self-similar for approximately 2 decades up to 10^{-3} V^2s. In some cases the scaling exponents deviate slightly from the value of -3/2 that has been predicted theoretically (Dahmen et al., 2011), observed in cellular automata models (Klein et al., 2017), and also proposed for natural seismicity (Kagan, 2010). Similar power law scaling of event sizes has been reported in several studies covering a variety of sample materials and apparatus (Baró et al., 2013; Dalton & Corcoran, 2001, 2002; Uhl et al., 2015; Johnson et al., 2013). Benzi et al. (2016) reported exponents in the range of -1.2 to -1.4 from numerical experiments on simulated soft glasses. An important question is whether one can use the distribution of event sizes to predict the maximum expected size. Our data show that using linear extrapolation to predict the sizes of events larger than 10^{-3} V^2s is not recommended, as it would either under- or overestimate the right-hand side tail of the distributions. Let us assume that events sizes are proportional to the product of the corresponding stress drop and slip. Then there is an obvious constraint for the maximum stress drop, i.e. a complete stress drop. However, the amount of slip cannot be constrained mechanistically. The available data merely show that higher normal stress allows the system to produce larger events (Figure 5).

Several laboratory studies have presented evidence of time-domain correlations, which are seen as evidence for complex dynamics (Davidsen et al., 2007; Baró et al., 2013; Lherminier et al., 2019). Spatial correlations have also been reported in granular systems (Denisov et al., 2016). Kumar et al. (2020) reported non-trivial space-time correlations in numerical and experimental systems, including the one discussed here.The distributions of normalized interevent times (Figure 6) and interevent distance $\Delta\theta$ (Figure 7) clearly reveal correlations between AE events. These correlations depend on the particle size range, as evidenced by the different shapes of the distributions. We attribute this to different geometric effects, such as packing ratio, between the two sample types. Factors that are known to affect the frictional strength and stability of sheared granular media include the width of the particle size distribution (Sammis et al., 1987; Morgan & Boettcher, 1999; Morgan, 1999; Mair et al., 2002), the packing ratio (Hayman et al., 2011; Aharonov & Sparks, 1999), and the roughness of the piston boundaries (Anthony & Marone, 2005). It is likely that both the relative range of particle sizes (150-212 μm versus 400-500 μm), in addition to the particles' relative size compared to the piston serrations resulted in different microstructures (i.e. arrangement of particles in space, which may vary from one locality to the next and over time within one sample) for the two sample types. However, the dominant style of sliding (regular versus irregular stick-slip) is (co-)determined by the applied normal stress (Figure 5, Figure 6). We posit that the primary contribution of higher normal stress in this context is not wear enhancement, but rather the concentration of elastic energy released from past events in a smaller region around their nucleation sites. Thus, subsequent events tend to nucleate from "hotspots", which may be responsible for the regular stick-slip behavior. We base this hypothesis on the shift of the red curve to the left, compared to the magenta curve, in Figure 7. Owens and Daniels (2011) demonstrated that local heterogeneities in the force-chain network control elastic wave propagation in granular packings.

The observed spontaneous transitions between regular and irregular stick-slip (Figure 3) suggest that the mode of sliding is also determined by factors that evolve during shearing. Previous studies have reported such transitions (Dalton & Corcoran, 2001; Geller et al., 2015; Hayman et al., 2011; Ben-Zion & Rice, 1993; Dahmen et al., 2011). We have attributed the end member modes we observed in our experiments to the initial particle size range and the applied normal stress. However, transient mode-switching would require reversible changes in the microstructure of the samples, since all other parameters (normal stress, rate of rotation, amount of sample material) remained constant. Postmortem visual inspection of our samples revealed that fines were generated during the experiments, likely as a result of abrasive wear (Figure 8). However the bulk of the sample material remained intact, which may explain the absence of long-term strengthening or weakening trends. Therefore, a plausible mechanistic explanation for transient mode switching is that local accumulations of fine particles temporarily altered the interactions between load-bearing particles and thus the macroscopic frictional behavior of the aggregate. "Local" accumulations may be understood either in the sense of a spatially limited heterogeneity in material properties along strike, e.g. a patch of granular aggregate with altered particle size distribution, or in the sense of a layer parallel to the frictional interface, e.g. a boundary shear. We have also considered the possibility that wear material trapped between the sidewalls that provide the sample with lateral support and the forcing pistons may have affected our measurements. However, the seals between the various components that the sample chamber is comprised of were thoroughly lubricated prior to each experiment. Furthermore, these seals were not under significant stress, especially compared to the values of normal stress used in our experiments.

In discussing the possible reasons for regular versus irregular stick-slip, we have assumed that the strength of the particles does not depend on their size for the range of sizes that we are dealing with. Furthermore, we have not explicitly considered time-dependent processes that have been shown to influence the frictional behavior of granular aggregates in discrete element method simulations (van den Ende & Niemeijer, 2018). However, time-dependent mechanisms are likely very slow under the conditions our experiments were performed at (Rossi et al., 2007).

4.2 The Effect of Torsional Stiffness

Our data show that lowering the torsional stiffness of the apparatus had little impact on the statistics of stick-slip (figures 5, 6, and 7). The only notable exception was shifting the right-hand side tail of AE size distribution to the right in the case of r066 (small particles; $\sigma_n = 4$ MPa). Additional experiments would help us evaluate how robust these observations are. The existing data suggest that either the effect of lowering the torsional stiffness is minimal compared to the effect of normal stress and particle size on sample rigidity, or that little of the extra elastic energy that is available to the system is released via AEs. The former scenario (i.e. small effect of apparatus stiffness) is in conflict with previous studies that clearly show the influence of stiffness on the frictional behavior of granular aggregates, albeit under different conditions and using different sample materials (Leeman et al., 2016; Murphy et al., 2019).

4.3 Comparison with Natural Seismicity

Our laboratory approach is a simplified analog of slowly driven systems that exhibit intermittent plasticity (Sethna et al., 2001). There is also a geometric similarity with faults that contain granular or pulverized wear materials. This study demonstrates that complex behavior can emerge from mechanical interactions without the need for accelerated chemical effects. In explaining natural seismicity there are numerous additional effects to consider, such as the presence of pore fluids, elevated temperature, chemical processes (Niemeijer et al., 2012) and complex fault zone geometry (Faulkner et al., 2010). Nevertheless, our findings provide some context for discussing complex, brittle behavior in the lithosphere.

The distributions of AE sizes (Figure 5) contain a power law segment, similar to the seismic moment distribution that describes natural seismicity (Ben-Zion, 2008). The power law exponent in some experiments is close to the value of -3/2 which has been proposed for natural seismicity (Kagan, 2010). Depending on the particle size range used and the applied normal stress, the right-hand side tail of the distributions is similar to either the Gutenberg-Richter model or the Characteristic Earthquake model (Wesnousky, 1994; Main, 1996). We also report correlations in the time domain (Figure 6). Natural seismicity exhibits similar features, namely the well-established Omori-Utsu law (Utsu et al., 1995) and the generalized gamma distribution of interevent times (Corral, 2004; Saichev & Sornette, 2007; Davidsen & Kwiatek, 2013; Kumar et al., 2020).

A major issue for seismic hazard analysis is the determination of the maximum expected seismic moment. This is related to the shape of the right tail of the seismic moment distribution. Parameters that control the truncation of the right-hand side tail of our AE size distributions are the applied normal stress and the particle size range, with an upper limit probably imposed by the size of the entire sample. System stiffness plays a subtle role in the experiments. Translating these parameters to factors in nature that control the truncation of the seismic moment distribution is not straightforward, excluding perhaps system size which can be translated to fault zone dimensions. The effect of normal stress is rather complex, as some of the largest earthquakes have occurred relatively shallow in the lithosphere. The geometry of faults and their internal structure and lithology may amplify stress locally, which could produce effects similar to what we observed in our experiments and attributed to the combination of normal stress and particle size range. Note that the participation of multiple faults in a single earthquake resulting in a larger earthquake than each individual fault is capable of producing on its own, as was the case for the 2016 M_w 7.8 Kaikoura earthquake (Shi et al., 2017; Lamb et al., 2018), is not explicitly modeled in our system. However, the emergent spatial correlations in our granular system can be considered as an analog and warrant further research regarding their temporal and spatial properties.

Another important point for seismic hazard analysis is the choice between the G-R and CE models. Closely related to this is the question of mode switching between the two models (Klügel, 2005, 2010; Ben-Zion, 2008). Our findings suggest that G-R or CE fault behavior depends on tunable parameters of the same system. We have also shown that the system may transition between the two (Figure 3). Williams et al. (2017) provide evidence that suggests such transitions may occur in nature as well. It is conceivable that slip on natural faults is dependent on some parameters that may evolve over time and/or accumulated slip. If that is the case, the characterization of faults based on the history of their activity for the purposes of seismic hazard assessment may in fact be futile. This is unfortunate because mistaking CE for G-R behavior may lead to significant underestimation of the frequency and maximum magnitude of big earthquakes. For known faults an alternative is to determine the maximum earthquake size possible based on fault dimensions (e.g., Trippetta et al., 2019).

5 Conclusions

To conclude, we have presented a laboratory system that can produce regular or irregular stick-slip depending on particle size distribution of the sample and the applied normal stress. This system is clearly far removed from the conditions prevailing in natural fault zones, in terms of stress, strain rate and chemical composition. Nevertheless, it is a slowly driven system that consists of many interacting agents (glass particles and the apparatus) and exhibits complex behavior. It can be considered in many respects as an analog for the slowly driven lithosphere that deforms intermittently via the interaction of multiple faults. In terms of the normal stress values used and the total shear displacement imposed, this study fills a gap in the existing literature on granular media.

The first key finding in relation to natural seismicity is that a single frictional interface can produce either CE or G-R size distributions. Second, stick-slip mode can switch during limited periods of observation (i.e. comparable to the long-term mean rate of occurrence). Taken together, these two results suggest that periods of observation comparable to the long-term rate of occurrence, as is the case with natural seismicity, could lead to false impressions about the style of moment release. The frictional strength and stability along a fault will likely change over time, via material wear during earthquakes and via healing during interseismic periods. Therefore we posit that for the purpose of PSHA, the question of whether a particular fault produces characteristic or Gutenberg-Richter-type seismicity may actually be impossible to answer. A physics- rather than a statistics-based seismic hazard analysis may thus be a necessary route forward.

Subsequent work on the experiment presented here can benefit from improvements in the accuracy and precision of shear stress and slip measurements. This would allow the study of the scaling between stress drops, slips, and AE size, in order to constrain the energy budget of the system and the role of torsional stiffness. It would also allow the comparison of friction values among different experiments. These topics are left for future work.

Appendix A Procedure for Locating AE Sources

The first step to calculating the source of an AE event is determining the first arrival time at every AE sensor. A reliable method for automatic first arrival picking of earthquake signals and AEs is based on the Akaike Information Criterion (Akaike, 1971). An AIC-based characteristic function can be evaluated by applying equation 2 from Zhang et al. (2003) on a seismogram:

$$AIC(x) = x \log_{10}(Var(s[1, x])) + (N - x - 1) \log_{10}(Var(s[x + 1, N])) \tag{A1}$$

where s is a seismogram of length N, and x is a variable that takes any value in the window $[1, N]$. The signal onset should coincide with the global minimum of the AIC function (Figure A1a, bottom panel). However, depending on the type of signal onset and the signal to noise ratio of the waveform, the global minimum of the AIC function may be shifted in time. To overcome this problem, the AIC formula should be computed only for the part of the seismogram that includes the signal's onset, instead of the entire seismogram. Perhaps the most commonly used method for seismic and acoustic event detection is some variation of the short-term/long-term average (STA/LTA) method (Allen, 1978). The downside of this method is that the analyst must choose the optimum lengths of the short- and long-term average windows and select a threshold value for automatic picking. Because the waveforms we recorded for each event differ in phase and amplitude depending on the distance of each receiver from the source, we opted for a more hands-off approach: higher order statistics have previously been used as a method for detecting the signal onset (Küperkoch et al., 2010). The expanding kurtosis of an AE waveform reaches its maximum shortly after the transition from noise to an AE signal. For each individual waveform, we calculated an expanding kurtosis function in order to estimate the approximate onset of the AE signal (Figure A1a, middle panel). Subsequently, we selected a 200 μs long window of the waveform, such that the window terminated at the onset time estimated by the peak of the expanding kurtosis function. The length of that window was preselected based on the dimensions of the sample and the expected maximum travel time between the source and the farthest receiver. We then applied the AIC formula to that subset of the waveform to obtain a more accurate onset time (Figure A1a, bottom panel). The accuracy of the picked onsets was improved by applying a low-pass filter (600 kHz cutoff frequency) to the waveforms before submitting them to the procedure described above.

The next step in locating the azimuth of the AE sources was the inversion of the observed arrival times to obtain a solution (t, ρ, v). Because the sample chamber is ring shaped, for each event we used picks from AE receivers located within line-of-sight of the approximate source location. This choice has two advantages: first, we do not have to search for complicated wave paths to account for the time delays observed in the onsets of the signals recorded at receivers located farther than about 70^o from the presumed source location; and, second, the receivers in the proximity of each AE event typically show high signal-to-noise ratio (SNR) and impulsive onsets compared to low SNR and emergent onsets at receivers farther away or on the far side of the piston rings (Figure A1b). High SNR and impulsive onsets present a more favorable scenario to both manual and automatic picking, resulting in more reliable picks. Due to the spacing of the AE receivers and depending on the relative offset of the top and bottom piston arrays at the time of the event, between 5 and 7 receivers receive a direct first wave from the source. For each event, we ran an iterative scheme that minimized the sum of the squared differences between observed and predicted onset times,

$$m_{(t,\theta,v)} = \sum_{i=1}^{n} (t_i^o - t_i^p)^2 \tag{A2}$$

where $m_{(t,\theta,v)}$ is the misfit at (t, θ, v), n is the total number of receivers used in the calculation, t_i^o is the observed arrival time at receiver i, and t_i^p is the predicted arrival time for receiver i. The scheme uses the BFGS method developed by Broyden, Fletcher, Goldfarb and Shanno (Nocedal & Wright, 2006). The predicted onset times correspond to direct waves in a single velocity model since the dominant wavelength of the AE signals is comparable to the dimensions of the structure in which the signals propagate. We obtained a measure of the uncertainty in each solution by estimating the standard errors of the parameters we inverted for $(t, \theta,$ and $v)$ from the Hessian matrix supplied by the BFGS minimizer. We report uncertainties as two standard deviations, i.e. twice the standard error of each parameter. Our criteria for accepting a solution are as follows: 1) the minimization must have terminated successfully, 2) the estimated t must be reasonable

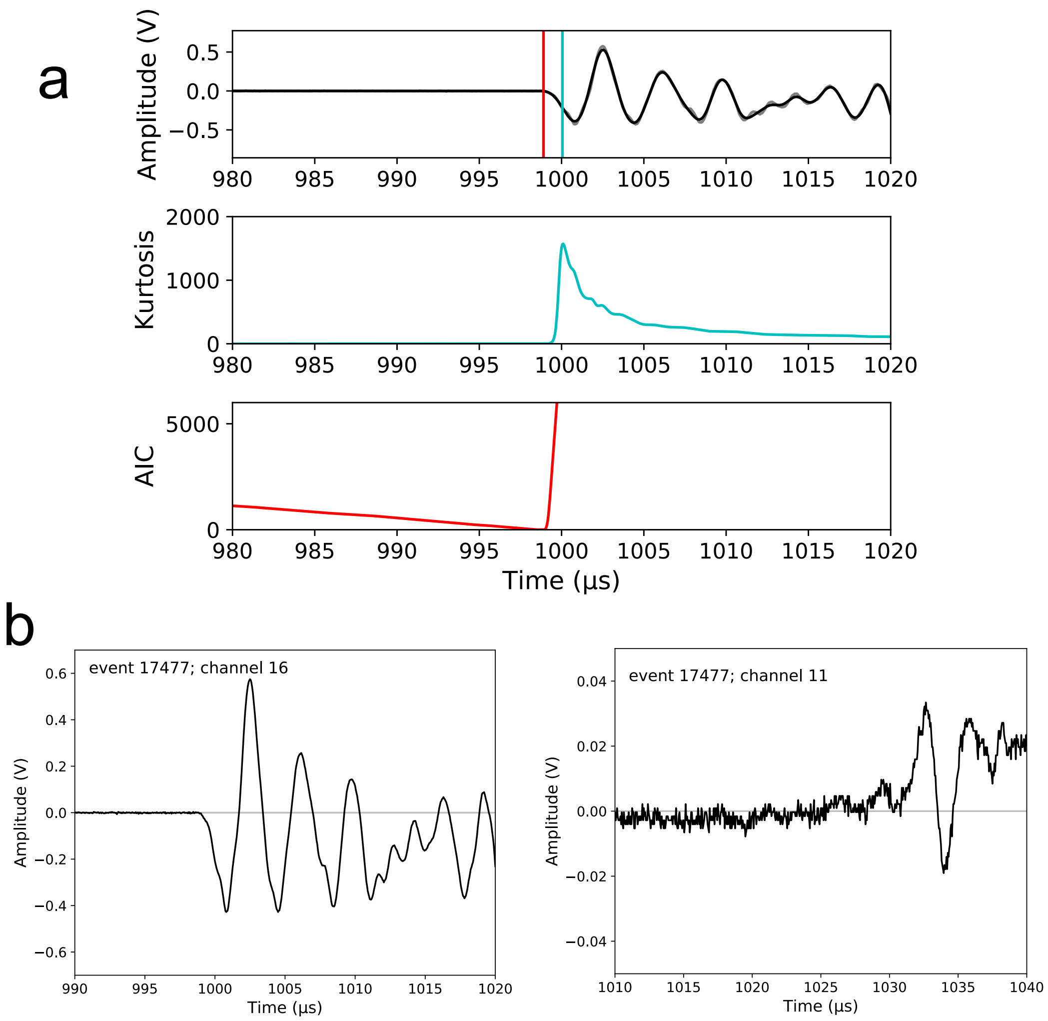

Figure A1. (a) Example of the automatic picking procedure. Data from experiment r086, event 17477, transducer 16 (top, stationary piston). (Top panel) Filtered signal (black), with kurtosis (cyan) and AIC (red) picks. A low pass Butterworth filter with 600 kHz corner frequency had been applied to the raw signal (grey) prior to the automatic picking procedure. (Middle panel) The expanding kurtosis characteristic function. (Bottom panel) The AIC characteristic function calculated for a portion of the signal. The first arrival corresponds to the global minimum of the AIC CF. (b) Comparison of signal onsets at two different transducers inside the top, stationary piston for event 17477. (Left) Impulsive onset recorded by the nearest transducer. (Right) Noisy signal and emergent onset (from about 1020 μs onward), recorded by the transducer that was positioned 135 degrees away from the one in the left panel. Figure from Korkolis (2019).

based on the dimensions of the sample and the maximum possible travel distance between the source and the nearest receiver (7 μs for about 10.6 mm at 1500 m/s), and 3) the estimated velocity must be positive and not exceed the longitudinal wave velocity in steel (about 5800 m/s).

We validated this method experimentally by performing glass capillary fracture tests between the steel piston rings. The fracture of a glass capillary produces a sharp force pulse that sends elastic waves through the steel pistons. The AE receivers record the signals and the resulting waveforms can be used to estimate the location of the fractured tube. By performing multiple tests at different locations along the piston rings and for various relative offsets between the top and bottom receiver arrays, we determined that the mean uncertainty in the source azimuth, given as 2 standard deviations, is about ± 3.5 degrees (± 2.6 mm).

Acknowledgments

We would like to thank Eimert de Graaff, Thony van der Gon Netscher, and Floris van Oort for providing technical support. The method for controlling the torsional stiffness of the apparatus was conceived by Martijn van den Ende. The sample material was provided by the Rock and Sediment Mechanics Laboratory at The Pennsylvania State University. This study was funded by ERC Starting Grant SEISMIC (335915). The data used in this study can be found at [TBD].

References

Aharonov, E., & Sparks, D. (1999). Rigidity phase transition in granular packings. *Physical Review E*, *60*(6), 6890–6896. doi: 10.1103/PhysRevE.60.6890

Akaike, H. (1971). Autoregressive model fitting for control. *Annals of the Institute of Statistical Mathematics*, *23*(1), 163–180. doi: 10.1007/BF02479221

Allen, R. V. (1978). Automatic earthquake recognition and timing from single traces. *Bulletin of the Seismological Society of America*, *68*(5), 1521–1532.

Anthony, J. L., & Marone, C. (2005). Influence of particle characteristics on granular friction. *Journal of Geophysical Research*, *110*(B8), B08409. doi: 10.1029/2004JB003399

Bakun, W. H., & Lindh, A. G. (1985). The Parkfield, California, Earthquake Prediction Experiment. *Science*, *229*(4714), 619–624. doi: 10.1126/science.229.4714.619

Barka, A. (1996). Slip distribution along the North Anatolian fault associated with the large earthquakes of the period 1939 to 1967. *Bulletin of the Seismological Society of America*, *86*(5), 1238–1254.

Baró, J., Corral, Á., Illa, X., Planes, A., Salje, E. K. H., Schranz, W., … Vives, E. (2013). Statistical Similarity between the Compression of a Porous Material and Earthquakes. *Physical Review Letters*, *110*(8), 088702. doi: 10.1103/PhysRevLett.110.088702

Ben-Zion, Y. (2008). Collective behavior of earthquakes and faults: Continuum-discrete transitions, progressive evolutionary changes, and different dynamic regimes. *Reviews of Geophysics*, *46*(4), RG4006. doi: 10.1029/2008RG000260

Ben-Zion, Y., & Rice, J. R. (1993). Earthquake failure sequences along a cellular fault zone in a three-dimensional elastic solid containing asperity and nonasperity regions. *Journal of Geophysical Research: Solid Earth*, *98*(B8), 14109–14131. doi: 10.1029/93JB01096

Ben-Zion, Y., & Rice, J. R. (1995). Slip patterns and earthquake populations along different classes of faults in elastic solids. *Journal of Geophysical Research: Solid Earth*, *100*(B7), 12959–12983. doi: 10.1029/94JB03037

Benzi, R., Kumar, P., Toschi, F., & Trampert, J. (2016). Earthquake statistics and plastic events in soft-glassy materials. *Geophysical Journal International*, *207*(3), 1667–1674. doi: 10.1093/gji/ggw366

Boettcher, M. S., & McGuire, J. J. (2009). Scaling relations for seismic cycles on mid-ocean ridge transform faults. *Geophysical Research Letters*, *36*(21), L21301. doi: 10.1029/2009GL040115

Brown, S. R., Scholz, C. H., & Rundle, J. B. (1991). A simplified spring-block model of earthquakes. *Geophysical Research Letters*, *18*(2), 215–218. doi: 10.1029/91GL00210

Carlson, J. M., & Langer, J. S. (1989). Mechanical model of an earthquake fault. *Physical Review A*, *40*(11), 6470–6484. doi: 10.1103/PhysRevA.40.6470

Cates, M. E., Wittmer, J. P., Bouchaud, J.-P., & Claudin, P. (1998). Jamming, Force Chains, and Fragile Matter. *Physical Review Letters*, *81*(9), 1841–1844. doi: 10.1103/PhysRevLett.81.1841

Corral, Á. (2004). Long-Term Clustering, Scaling, and Universality in the Temporal Occurrence of Earthquakes. *Physical Review Letters*, *92*(10), 108501. doi: 10.1103/PhysRevLett.92.108501

Cui, D., Wu, W., Xiang, W., Doanh, T., Chen, Q., Wang, S., ... Wang, J. (2017). Stick-slip behaviours of dry glass beads in triaxial compression. *Granular Matter*, *19*(1), 1. doi: 10.1007/s10035-016-0682-5

Dahmen, K. A., Ben-Zion, Y., & Uhl, J. T. (2011). A simple analytic theory for the statistics of avalanches in sheared granular materials. *Nature Physics*, *7*(7), 554–557. doi: 10.1038/nphys1957

Dahmen, K. A., Ertaş, D., & Ben-Zion, Y. (1998). Gutenberg-Richter and characteristic earthquake behavior in simple mean-field models of heterogeneous faults. *Physical Review E*, *58*(2), 1494–1501. doi: 10.1103/PhysRevE.58.1494

Dalton, F., & Corcoran, D. (2001). Self-organized criticality in a sheared granular stick-slip system. *Physical Review E*, *63*(6), 061312. doi: 10.1103/PhysRevE.63.061312

Dalton, F., & Corcoran, D. (2002). Basin of attraction of a bounded self-organized critical state. *Physical Review E*, *65*(3), 031310. doi: 10.1103/PhysRevE.65.031310

Davidsen, J., & Kwiatek, G. (2013). Earthquake Interevent Time Distribution for Induced Micro-, Nano-, and Picoseismicity. *Physical Review Letters*, *110*(6), 068501. doi: 10.1103/PhysRevLett.110.068501

Davidsen, J., Stanchits, S., & Dresen, G. (2007). Scaling and Universality in Rock Fracture. *Physical Review Letters*, *98*(12), 125502. doi: 10.1103/PhysRevLett.98.125502

Denisov, D. V., Lörincz, K. A., Uhl, J. T., Dahmen, K. A., & Schall, P. (2016). Universality of slip avalanches in flowing granular matter. *Nature Communications*, *7*(1), 10641. doi: 10.1038/ncomms10641

Faulkner, D., Jackson, C., Lunn, R., Schlische, R., Shipton, Z., Wibberley, C., & Withjack, M. (2010). A review of recent developments concerning the structure, mechanics and fluid flow properties of fault zones. *Journal of Structural Geology*, *32*(11), 1557–1575. doi: 10.1016/j.jsg.2010.06.009

Ferdowsi, B., Griffa, M., Guyer, R. A., Johnson, P. A., Marone, C., & Carmeliet, J. (2013). Microslips as precursors of large slip events in the stick-slip dynamics of sheared granular layers: A discrete element model analysis. *Geophysical Research Letters*, *40*(16), 4194–4198. doi: 10.1002/grl.50813

Field, E. H., Jordan, T. H., Page, M. T., Milner, K. R., Shaw, B. E., Dawson, T. E., ... Thatcher, W. R. (2017). A Synoptic View of the Third Uniform California Earthquake Rupture Forecast (UCERF3). *Seismological Research Letters*, *88*(5), 1259–1267. doi: 10.1785/0220170045

Furlong, K. P., & Herman, M. (2017). Reconciling the deformational dichotomy of the 2016 M_w 7.8 Kaikoura New Zealand earthquake. *Geophysical Research Letters*, *44*(13), 6788–6791. doi: 10.1002/2017GL074365

Geller, D. A., Ecke, R. E., Dahmen, K. A., & Backhaus, S. (2015). Stick-slip behavior in a continuum-granular experiment. *Physical Review E*, *92*(6), 060201. doi: 10.1103/PhysRevE.92.060201

Guo, Y., & Morgan, J. K. (2007). Fault gouge evolution and its dependence on normal stress and rock strength—Results of discrete element simulations: Gouge zone properties. *Journal of Geophysical Research*, *112*(B10), B10403. doi: 10.1029/2006JB004524

Hamilton, T., & McCloskey, J. (1997). Breakdown in power-law scaling in an analogue model of earthquake rupture and stick-slip. *Geophysical Research Letters*, *24*(4), 465–468. doi: 10.1029/97GL00203

Hayman, N. W., Ducloué, L., Foco, K. L., & Daniels, K. E. (2011). Granular Controls on Periodicity of Stick-Slip Events: Kinematics and Force-Chains in an Experimental Fault. *Pure and Applied Geophysics*, *168*(12), 2239–2257. doi: 10.1007/s00024-011-0269-3

Jaeger, H. M., Nagel, S. R., & Behringer, R. P. (1996). Granular solids, liquids, and gases. *Reviews of Modern Physics*, *68*(4), 1259–1273. doi: 10.1103/RevModPhys.68.1259

Jiang, Y., Wang, G., & Kamai, T. (2017). Acoustic emission signature of mechanical failure: Insights from ring-shear friction experiments on granular materials: AE Signature of Mechanical Failure. *Geophysical Research Letters*, *44*(6), 2782–2791. doi: 10.1002/2016GL071196

Johnson, P. A., Ferdowsi, B., Kaproth, B. M., Scuderi, M., Griffa, M., Carmeliet, J., ... Marone, C. (2013). Acoustic emission and microslip precursors to stick-slip failure in sheared granular material. *Geophysical Research Letters*, *40*(21), 5627–5631. doi: 10.1002/2013GL057848

Kagan, Y. Y. (1993). Statistics of characteristic earthquakes. *Bulletin of the Seismological Society of America*, *83*(1), 7–24.

Kagan, Y. Y. (1994). Observational evidence for earthquakes as a nonlinear dynamic process. *Physica D: Nonlinear Phenomena*, *77*(1-3), 160–192. doi: 10.1016/0167-2789(94)90132-5

Kagan, Y. Y. (1996). Comment on "The Gutenberg-Richter or characteristic earthquake distribution, which is it?" by Steven G. Wesnousky. *Bulletin of the Seismological Society of America*, *86*(1A), 274–285.

Kagan, Y. Y. (2010). Earthquake size distribution: Power-law with exponent $B \equiv 1/2$? *Tectonophysics*, *490*(1-2), 103–114. doi: 10.1016/j.tecto.2010.04.034

Kagan, Y. Y., & Jackson, D. D. (1991). Seismic Gap Hypothesis: Ten years after. *Journal of Geophysical Research: Solid Earth*, *96*(B13), 21419–21431. doi: 10.1029/91JB02210

Kagan, Y. Y., & Jackson, D. D. (1995). New seismic gap hypothesis: Five years after. *Journal of Geophysical Research: Solid Earth*, *100*(B3), 3943–3959. doi: 10.1029/94JB03014

Kagan, Y. Y., & Jackson, D. D. (1999). Worldwide doublets of large shallow earthquakes. *Bulletin of the Seismological Society of America*, *89*(5), 1147–1155.

Kagan, Y. Y., & Jackson, D. D. (2013). Tohoku Earthquake: A Surprise? *Bulletin of the Seismological Society of America*, *103*(2B), 1181–1194. doi: 10.1785/0120120110

Kagan, Y. Y., Jackson, D. D., & Geller, R. J. (2012). Characteristic Earthquake Model, 1884-2011, R.I.P. *Seismological Research Letters*, *83*(6), 951–953. doi: 10.1785/0220120107

Kanamori, H., & Brodsky, E. E. (2004). The physics of earthquakes. *Reports on Progress in Physics*, *67*(8), 1429–1496. doi: 10.1088/0034-4885/67/8/R03

Klein, W., Gould, H., Tiampo, K. F., Silva, J. B., Gu, T., Kazemian, J., ... Rundle, J. B. (2017). Statistical Mechanics Perspective on Earthquakes. In E. K. Salje, A. Saxena, & A. Planes (Eds.), *Avalanches in Functional Materials and Geophysics* (pp. 1–18). Cham: Springer International Publishing. doi: 10.1007/978-3-319-45612-6_1

Klügel, J.-U. (2005). Problems in the application of the SSHAC probability method for assessing earthquake hazards at Swiss nuclear power plants. *Engineering Geology*, *78*(3-4), 285–307. doi: 10.1016/j.enggeo.2005.01.007

Klügel, J.-U. (2010). Comment on "Is There a Basis for Preferring Characteristic Earthquakes over a Gutenberg-Richter Distribution in Probabilistic Earthquake Forecasting" by Tom Parsons and Eric L. Geist. *Bulletin of the Seismological Society of America*, *100*(2), 896–897. doi: 10.1785/0120090170

Korkolis, E. (2019). *Rotary shear experiments on glass bead aggregates: Stick-slip statistics and parallels with natural seismicity* (First ed., Vol. 195). Utrecht.

Kumar, P., Korkolis, E., Benzi, R., Denisov, D., Niemeijer, A., Schall, P., ... Trampert, J. (2020). On interevent time distributions of avalanche dynamics. *Scientific Reports*, *10*(1), 626. doi: 10.1038/s41598-019-56764-6

Küperkoch, L., Meier, T., Lee, J., Friederich, W., & Working Group, E. (2010). Automated determination of P -phase arrival times at regional and local distances using higher order statistics. *Geophysical Journal International*. doi: 10.1111/j.1365-246X.2010.04570.x

Lamb, S., Arnold, R., & Moore, J. D. P. (2018). Locking on a megathrust as a cause of distributed faulting and fault-jumping earthquakes. *Nature Geoscience*, *11*(11), 871–875. doi: 10.1038/s41561-018-0230-5

Leeman, J. R., Saffer, D. M., Scuderi, M. M., & Marone, C. (2016). Laboratory observations of slow earthquakes and the spectrum of tectonic fault slip modes. *Nature Communications*, *7*(1), 11104. doi: 10.1038/ncomms11104

Lherminier, S., Planet, R., dit Vehel, V. L., Simon, G., Vanel, L., Måløy, K. J., & Ramos, O. (2019). Continuously Sheared Granular Matter Reproduces in Detail Seismicity Laws. *Physical Review Letters*, *122*(21), 218501. doi: 10.1103/PhysRevLett.122.218501

Main, I. (1996). Statistical physics, seismogenesis, and seismic hazard. *Reviews of Geophysics*, *34*(4), 433–462. doi: 10.1029/96RG02808

Mair, K., Frye, K. M., & Marone, C. (2002). Influence of grain characteristics on the friction of granular shear zones: Grain shape influence on friction. *Journal of Geophysical Research: Solid Earth*, *107*(B10), ECV 4-1-ECV 4-9. doi: 10.1029/2001JB000516

Mair, K., & Hazzard, J. F. (2007). Nature of stress accommodation in sheared granular material: Insights from 3D numerical modeling. *Earth and Planetary Science Letters*, *259*(3-4), 469–485. doi: 10.1016/j.epsl.2007.05.006

McGuire, J. J. (2008). Seismic Cycles and Earthquake Predictability on East Pacific Rise Transform Faults. *Bulletin of the Seismological Society of America*, *98*(3), 1067–1084. doi: 10.1785/0120070154

McGuire, J. J., Collins, J. A., Gouédard, P., Roland, E., Lizarralde, D., Boettcher, M. S., ... van der Hilst, R. D. (2012). Variations in earthquake rupture properties along the Gofar transform fault, East Pacific Rise. *Nature Geoscience*, *5*(5), 336–341. doi: 10.1038/ngeo1454

Morgan, J. K. (1999). Numerical simulations of granular shear zones using the distinct element method: 2. Effects of particle size distribution and interparticle friction on mechanical behavior. *Journal of Geophysical Research: Solid Earth*, *104*(B2), 2721–2732. doi: 10.1029/1998JB900055

Morgan, J. K. (2004). Particle Dynamics Simulations of Rate- and State-dependent Frictional Sliding of Granular Fault Gouge. *Pure and Applied Geophysics*, *161*(9-10). doi: 10.1007/s00024-004-2537-y

Morgan, J. K., & Boettcher, M. S. (1999). Numerical simulations of granular shear zones using the distinct element method: 1. Shear zone kinematics and the micromechanics of localization. *Journal of Geophysical Research: Solid Earth*, *104*(B2), 2703–2719. doi: 10.1029/1998JB900056

Mulargia, F., Stark, P. B., & Geller, R. J. (2017). Why is Probabilistic Seismic Hazard Analysis (PSHA) still used? *Physics of the Earth and Planetary Interiors*, *264*, 63–75. doi: 10.1016/j.pepi.2016.12.002

Murphy, K. A., Dahmen, K. A., & Jaeger, H. M. (2019). Transforming Mesoscale Granular Plasticity Through Particle Shape. *Physical Review X*, *9*(1), 011014. doi: 10.1103/PhysRevX.9.011014

Nasuno, S., Kudrolli, A., & Gollub, J. P. (1997). Friction in Granular Layers: Hysteresis and Precursors. *Physical Review Letters*, *79*(5), 949–952. doi: 10.1103/PhysRevLett.79.949

Niemeijer, A., Di Toro, G., Griffith, W. A., Bistacchi, A., Smith, S. A., & Nielsen, S. (2012). Inferring earthquake physics and chemistry using an integrated field and laboratory approach. *Journal of Structural Geology*, *39*, 2–36. doi: 10.1016/j.jsg.2012.02.018

Nocedal, J., & Wright, S. J. (2006). *Numerical Optimization.* Springer New York. doi: 10.1007/978-0-387-40065-5

Owens, E. T., & Daniels, K. E. (2011). Sound propagation and force chains in granular materials. *EPL (Europhysics Letters)*, *94*(5), 54005. doi: 10.1209/0295-5075/94/54005

Parsons, T., Console, R., Falcone, G., Murru, M., & Yamashina, K. (2012). Comparison of characteristic and Gutenberg-Richter models for time-dependent M $\geq$ 7.9 earthquake probability in the Nankai-Tokai subduction zone, Japan: Earthquake forecasts in the Tokai area. *Geophysical Journal International*, *190*(3), 1673–1688. doi: 10.1111/j.1365-246X.2012.05595.x

Parsons, T., & Geist, E. L. (2009). Is There a Basis for Preferring Characteristic Earthquakes over a Gutenberg-Richter Distribution in Probabilistic Earthquake Forecasting? *Bulletin of the Seismological Society of America*, *99*(3), 2012–2019. doi: 10.1785/0120080069

Parsons, T., Geist, E. L., Console, R., & Carluccio, R. (2018). Characteristic Earthquake Magnitude Frequency Distributions on Faults Calculated From Consensus Data in California. *Journal of Geophysical Research: Solid Earth*, 2018JB016539. doi: 10.1029/2018JB016539

Rong, Y., Jackson, D. D., & Kagan, Y. Y. (2003). Seismic gaps and earthquakes. *Journal of Geophysical Research: Solid Earth*, *108*(B10). doi: 10.1029/2002JB002334

Rossi, M., Vidal, O., Wunder, B., & Renard, F. (2007). Influence of time, temperature, confining pressure and fluid content on the experimental compaction of spherical grains. *Tectonophysics*, *441*(1-4), 47–65. doi: 10.1016/j.tecto.2007.05.001

Sachs, M. K., Yoder, M. R., Turcotte, D. L., Rundle, J. B., & Malamud, B. D. (2012). Black swans, power laws, and dragon-kings: Earthquakes, volcanic eruptions, landslides, wildfires, floods, and SOC models. *The European Physical Journal Special Topics*, *205*(1), 167–182. doi: 10.1140/epjst/e2012-01569-3

Saichev, A., & Sornette, D. (2007). Theory of earthquake recurrence times. *Journal of Geophysical Research: Solid Earth*, *112*(B4), B04313. doi: 10.1029/2006JB004536

Sammis, C., King, G., & Biegel, R. (1987). The kinematics of gouge deformation. *Pure and Applied Geophysics*, *125*(5), 777–812. doi: 10.1007/BF00878033

Savage, J. C. (1993). The Parkfield prediction fallacy. *Bulletin of the Seismological Society of America*, *83*(1), 1–6.

Schwartz, D. P., & Coppersmith, K. J. (1984). Fault behavior and characteristic earthquakes: Examples from the Wasatch and San Andreas Fault Zones. *Journal of Geophysical Research: Solid Earth*, *89*(B7), 5681–5698. doi: 10.1029/JB089iB07p05681

Scuderi, M. M., Carpenter, B. M., Johnson, P. A., & Marone, C. (2015). Poromechanics of stick-slip frictional sliding and strength recovery on tectonic faults. *Journal of Geophysical Research: Solid Earth*, *120*(10), 6895–6912. doi:

10.1002/2015JB011983
Scuderi, M. M., Carpenter, B. M., & Marone, C. (2014). Physicochemical processes of frictional healing: Effects of water on stick-slip stress drop and friction of granular fault gouge. *Journal of Geophysical Research: Solid Earth*, *119*(5), 4090–4105. doi: 10.1002/2013JB010641
Sethna, J. P., Dahmen, K. A., & Myers, C. R. (2001). Crackling noise. *Nature*, *410*(6825), 242–250. doi: 10.1038/35065675
Shcherbakov, R., Turcotte, D., & Rundle, J. (2015). Complexity and Earthquakes. In *Treatise on Geophysics* (pp. 627–653). Elsevier. doi: 10.1016/B978-0-444-53802-4.00094-4
Shi, X., Wang, Y., Liu-Zeng, J., Weldon, R., Wei, S., Wang, T., & Sieh, K. (2017). How complex is the 2016 M w 7.8 Kaikoura earthquake, South Island, New Zealand? *Science Bulletin*, *62*(5), 309–311. doi: 10.1016/j.scib.2017.01.033
Sornette, D., & Ouillon, G. (2012). Dragon-kings: Mechanisms, statistical methods and empirical evidence. *The European Physical Journal Special Topics*, *205*(1), 1–26. doi: 10.1140/epjst/e2012-01559-5
Sornette, D., & Sornette, A. (1999). General theory of the modified Gutenberg-Richter law for large seismic moments. *Bulletin of the Seismological Society of America*, *89*(4), 1121–1130.
Stein, S., & Friedrich, A. M. (2014). How much can we clear the crystal ball? *Astronomy & Geophysics*, *55*(2), 2.11-2.17. doi: 10.1093/astrogeo/atu076
Stein, S., Geller, R., & Liu, M. (2011). Bad Assumptions or Bad Luck: Why Earthquake Hazard Maps Need Objective Testing. *Seismological Research Letters*, *82*(5), 623–626. doi: 10.1785/gssrl.82.5.623
Stein, S., Geller, R. J., & Liu, M. (2012). Why earthquake hazard maps often fail and what to do about it. *Tectonophysics*, *562-563*, 1–25. doi: 10.1016/j.tecto.2012.06.047
Stirling, M. W. (2014). The Continued Utility of Probabilistic Seismic-Hazard Assessment. In *Earthquake Hazard, Risk and Disasters* (pp. 359–376). Elsevier. doi: 10.1016/B978-0-12-394848-9.00013-4
Swafford, L., & Stein, S. (2007). Limitations of the short earthquake record for seismicity and seismic hazard studies. In *Continental Intraplate Earthquakes: Science, Hazard, and Policy Issues.* Geological Society of America. doi: 10.1130/2007.2425(04)
Toksöz, M. N., Shakal, A. F., & Michael, A. J. (1979). Space-time migration of earthquakes along the North Anatolian fault zone and seismic gaps. *Pure and Applied Geophysics*, *117*(6), 1258–1270. doi: 10.1007/BF00876218
Trippetta, F., Petricca, P., Billi, A., Collettini, C., Cuffaro, M., Lombardi, A. M., ... Doglioni, C. (2019). From mapped faults to fault-length earthquake magnitude (FLEM): A test on Italy with methodological implications. *Solid Earth*, *10*(5), 1555–1579. doi: 10.5194/se-10-1555-2019
Uhl, J. T., Pathak, S., Schorlemmer, D., Liu, X., Swindeman, R., Brinkman, B. A. W., ... Dahmen, K. A. (2015). Universal Quake Statistics: From Compressed Nanocrystals to Earthquakes. *Scientific Reports*, *5*(1), 16493. doi: 10.1038/srep16493
Utsu, T., Ogata, Y., & Matsu'ura, R. S. (1995). The Centenary of the Omori Formula for a Decay Law of Aftershock Activity. *Journal of Physics of the Earth*, *43*(1), 1–33. doi: 10.4294/jpe1952.43.1
van den Ende, M., Chen, J., Ampuero, J.-P., & Niemeijer, A. (2018). A comparison between rate-and-state friction and microphysical models, based on numerical simulations of fault slip. *Tectonophysics*, *733*, 273–295. doi: 10.1016/j.tecto.2017.11.040
van den Ende, M., & Niemeijer, A. R. (2018). Time-Dependent Compaction as a Mechanism for Regular Stick-Slips. *Geophysical Research Letters*, *45*(12), 5959–5967. doi: 10.1029/2018GL078103

Weldon, R., Scharer, K., Fumal, T. E., & Biasi, G. (2004). Wrightwood and the earthquake cycle: What a long recurrence record tells us about how faults work. *GSA Today*, *14*, 4–10.

Wesnousky, S. G. (1994). The Gutenberg-Richter or characteristic earthquake distribution, which is it? *Bulletin of the Seismological Society of America*, *84*(6), 1940–1959.

Williams, R. T., Goodwin, L. B., Sharp, W. D., & Mozley, P. S. (2017). Reading a 400,000-year record of earthquake frequency for an intraplate fault. *Proceedings of the National Academy of Sciences*, *114*(19), 4893–4898. doi: 10.1073/pnas.1617945114

Wolfson-Schwehr, M., Boettcher, M. S., McGuire, J. J., & Collins, J. A. (2014). The relationship between seismicity and fault structure on the Discovery transform fault, East Pacific Rise. *Geochemistry, Geophysics, Geosystems*, *15*(9), 3698–3712. doi: 10.1002/2014GC005445

Zhang, H., Thurber, C., & Rowe, C. (2003). Automatic P-Wave Arrival Detection and Picking with Multiscale Wavelet Analysis for Single-Component Recordings. *Bulletin of the Seismological Society of America*, *93*(5), 1904–1912. doi: 10.1785/0120020241